

Nanohardness from First Principles with Active Learning on Atomic Environments

Evgeny V. Podryabinkin,* Alexander G. Kvashnin, Milad Asgarpour, Igor I. Maslenikov, Danila A. Ovsyannikov, Pavel B. Sorokin, Mikhail Yu Popov, and Alexander V. Shapeev



Cite This: <https://doi.org/10.1021/acs.jctc.1c00783>



Read Online

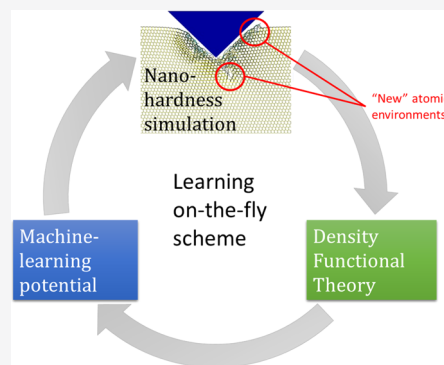
ACCESS |

Metrics & More

Article Recommendations

Supporting Information

ABSTRACT: We propose a methodology for the calculation of nanohardness by atomistic simulations of nanoindentation. The methodology is enabled by machine-learning interatomic potentials fitted on the fly to quantum-mechanical calculations of local fragments of the large nanoindentation simulation. We test our methodology by calculating nanohardness, as a function of load and crystallographic orientation of the surface, of diamond, AlN, SiC, BC₂N, and Si and comparing it to the calibrated values of the macro- and microhardness. The observed agreement between the computational and experimental results from the literature provides evidence that our method has sufficient predictive power to open up the possibility of designing materials with exceptional hardness directly from first principles. It will be especially valuable at the nanoscale where the experimental measurements are difficult, while empirical models fitted to macrohardness are, as a rule, inapplicable.



1. INTRODUCTION

Hardness is one of the most important properties of structural materials, quantifying their ability to resist indenting or scratching. The determination of hardness is traditionally based on the experimental measurement procedure during which the studied material is indented with a harder material, usually diamond. In this case, the hardness value itself is calculated as the ratio between the maximum indentation force and the area of the imprint left on the studied sample.

It should be noted that hardness is not a universal value and depends even on the shape of indenter.¹ The most common indenter shapes are ball (Brinell hardness²), square-based pyramid-shaped diamond indenter (Vickers hardness³), and three-sided pyramid (Berkovich hardness⁴). However, the measured hardness depends not only on the shape of the indenter but also on the depth of its penetration (or the scale of the measurements).^{1,4,5} For example, when measuring the hardness of metals at the macrolevel (maximum load ranges between 10 and 200 N),¹ the plasticity effects associated with the motion of grain boundaries play a decisive role. When measuring the hardness of a single crystal at the microlevel, the applied maximum load usually varies from 10 to 200 mN.¹ During such measurements, dislocations and other defects are formed. Their evolution and interaction under the action of elastic stress fields largely determine the resulting hardness. Finally, if the penetration depth is only a few nanometers (maximum load varies between tens of μN and 200 mN),¹ the imprint is mainly formed due to the migration of atoms displaced by the indenter. Thus, it is important to distinguish between macro-, micro-, and nanohardness (the scale of impact

of particular effects depends on the material being tested and many other factors).¹ Macrohardness is typically independent of the applied load or depth of penetration, whereas at the micro- and nanolevels, such dependence is substantial.¹ This effect is known as the “indentation size effect”^{1,6}. A possible explanation for this effect comes from the intrinsic structural factors of the studied specimens like high elastic recoveries, pileup, lack of dislocations at small indentations, work hardening, and the presence of grain precipitates.^{1,7} These effects are important and should be taken into account in the design of the films and coatings.^{8–10}

The smaller the scale of measurement is, the more complicated and expensive the experiment is. Hardness measurements at the nanoscale require high purity of the samples being studied and complex high-precision equipment, which should be accurately tuned. The mechanical vibrations during the measurements could bring additional artifacts and thus should be eliminated.¹¹ But even if these conditions are met, then the experiment is affected by other adverse factors: the interaction of the studied material with the material of the indenter, defects of the crystal lattice, degradation of the indenter, etc. Obviously, the smaller the measurement scale is,

Received: August 4, 2021

the stronger is the influence of such factors on the measurement results.

Experimental measurements are not the only way to assess hardness. They may be inefficient because of high cost, or simply not possible: for example, in computational materials design, the sample may be computer-generated and needs to be assessed before it is synthesized. Instead, a fast assessment of the hardness is typically done by empirical models based on various characteristics of the material, including bond length, electronegativity, bond strength, etc.^{12–14} Some of the models^{15,16} fit experimental data using mechanical characteristics of materials (bulk and shear moduli, Poisson ratio, etc.) as descriptors. All of these models are constructed as explicit formulae approximating known experimental data. None of these hardness models take into account the anisotropy of the crystal. At the same time, the hardness of diamond, for example, measured in different crystallographic directions, may differ by as much as 50%.^{17,18} Moreover, the hardness of layered structures may vary by several times in the same material depending on orientation due to the weak interlayer binding and the strong inlayer one.¹⁹ Because of the above, empirical models of hardness are not always in good agreement with the experimental data.

Macro- (and sometimes microhardness) can be calculated with continuum models, based on solving elastoplasticity equations. However, this method requires the knowledge of materials properties (namely, the dependence of elastic moduli on stress) and thus cannot be used for the prediction of the hardness of the materials for which these data are unknown. The conventional theory of elastoplasticity cannot be used as well for the hardness calculation at the nanoscale since homogeneity and continuity assumptions would be violated.^{1,20} Calculation of nanohardness requires describing complex mechanical processes such as the motion of dislocations and other defects, bond breaking, or displacement of atoms.

Atomistic simulations appear to be the only computational approach capable of capturing the complexity of hardness. Indeed, many works used molecular dynamics simulations to study nanoindentation of various materials at the atomic level, i.e., see refs 21–25. For example, in ref 21, the simulations of nanoindentation were done for layered heterostructures made of nanotwinned Cu/Ni layers. In ref 23, the authors simulated nanoindentation of diamond surfaces using modified Tersoff potentials and estimated the nanohardness anisotropy of diamond. However, the accuracy of atomistic simulations is typically limited by the accuracy of the potential of interatomic interaction. Traditionally, such potentials are developed using empirical data about the material (e.g., average interatomic distance, elastic moduli, thermal expansion, melting point, etc.) or using data from ab initio calculations. Therefore, classical empirical potentials typically reproduce the properties which they were fit to (and at the same conditions), and may not provide acceptable accuracy for the prediction of the complex properties of the materials or the simulation of some complex processes such as nanoindentation. To summarize, using empirical potentials for hardness calculation has three main disadvantages:

- a possibly large error, which is difficult to estimate;
- the accuracy is different for different compounds (since the potentials are often constructed using different approaches);
- empirical potentials have not been developed for many compounds.

In this work, we propose a nanohardness calculation method based on machine-learning interatomic potentials (MLIPs) overcoming the above difficulties. We are motivated by the field of computational design of novel materials in which one would need to assess the nanohardness of the newly computer-generated material candidate from first principles, without relying on the existing empirical information.

The proposed method is based on atomistic simulations of nanoindentation that not only allows for a fast and inexpensive estimation of nanohardness (compared to an experiment) but also lacks the adverse impact of external factors inevitably present in the experiment. The crucial component of the proposed approach is the model of interatomic interaction. Unfortunately, density functional theory (DFT), a well-validated model often giving accurate quantitative predictions, is prohibitively expensive for direct simulation of nanoindentation due to the need to take large sizes of the atomistic system. Machine-learning interatomic potentials (MLIPs) trained on DFT calculations have recently been proposed as a promising way forward in such problems. The key feature of MLIPs that distinguishes them from the classical potentials is their ability to approximate any interatomic interaction model with arbitrary accuracy (at least theoretically) with the increase of the number of parameters. Therefore, the performance of MLIPs is comparable with empirical potentials, and the accuracy is close to that of quantum-mechanical models. A number of MLIPs have been tested in various applications of computational material science, such as structure prediction,^{26–31} phase transitions and chemical reactions,^{32–35} calculation of mechanical and thermodynamic properties,^{36–41} etc.; in all of these applications, MLIPs showed an outstanding efficiency. In this work, we used moment tensor potentials (MTPs)^{28,42} implemented in ref 43, which are one of the state-of-the-art machine-learning models of interatomic interaction.^{44,45}

A major challenge in using MLIPs is reliability: MLIPs, to an even greater extent than empirical potentials, suffer from the transferability issue. Being trained on some atomistic configurations (the training set), MLIPs reproduce well the properties of similar configurations but may have poor accuracy for the configurations that significantly differ from the training set. Therefore, a rule of thumb for constructing a good training set is to include into it only relevant configurations, i.e., similar (in some sense) to those which will be evaluated during simulation.⁴⁶ In other words, the configurations in the training set must be sampled from the domain of configurational space containing the simulation trajectory (e.g., molecular dynamics trajectory or relaxation trajectory). If this domain is not fully represented in the training set, MLIP may extrapolate when calculating energy, forces, and stresses. This typically leads to a significant decrease in the accuracy and may cause instability of atomistic simulation. For example, uncontrolled extrapolation during relaxation may result in local energy minima with unphysically short interatomic distances. It will never happen if all of the configurations in the relaxation trajectory are interpolative, and similar configurations are represented in the training set. At the same time, to fit a good MLIP, the training set should not contain configurations that can never be met during evaluation (for example, graphene structures should not be included in the training set, if an MLIP is designed for simulating bulk diamond). The presence of such configurations does not trigger extrapolation; however, the interpolation error may decrease due to excessive expansion of the training domain.

A possible way to construct an optimal training set is learning on the fly. In our previous works, we have proposed⁴⁶ and applied^{28,29,32} active learning techniques to train MTPs (this approach can be applied to other MLIPs as well) on the fly. This approach involves a mechanism detecting configurations that trigger extrapolation when MLIP calculates their energy. If such an “extrapolative” configuration is met, it is added to the training set (with the DFT values of the energy and forces calculated), and the MLIP is retrained. This solution, however, cannot be implemented directly for hardness simulations because, in the context of this problem, we deal with large configurations that are out of reach for DFT calculations. In this work, as a crucial part of the proposed hardness calculation methodology, we also present a method aimed at solving this problem, which is based on detecting extrapolation on the local atomistic environments. If an extrapolative environment is encountered, it is treated as configurations with no periodicity (as an atomic cluster in vacuum) at the DFT calculation stage. This methodology enables active learning on the fly during simulation systems with many atoms.

2. NANOHARDNESS CALCULATION PROCEDURE

2.1. Simulation Setup. The proposed nanohardness calculation procedure is based on atomistic simulations of the nanoindentation test (see Figure 1). The studied sample

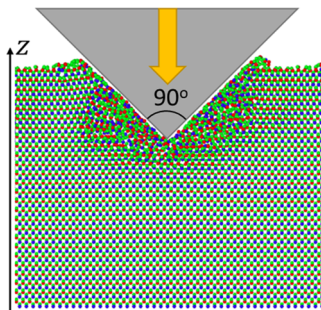


Figure 1. Schematic illustration of a nanoindentation simulation.

consists of atoms in a computational domain of parallelepiped shape. The system is periodic in x and y axes. The surfaces of the sample normal to the z -axis are free (see Figure 1). The motion of the bottom atomic layer is constrained: displacement of the bottom atoms along the z -axis is not allowed (but they can move in the x,y -plane).

In the experimental and theoretical studies, various shapes of a tip are used: spherical, conical, three- or four-sided pyramids, bricks, etc. To avoid the dependence of the calculation results on the size of the indenter and its orientation with respect to the crystallographic directions, we considered a conical shape with the apex angle of 90° as a trade-off between sharp cones wedging the material and leading to the early appearance of cracks and blunt cones, causing excessive compression of the material.

Interaction between atoms of the indenter and the studied material may also bring an undesirable dependency of the measured hardness on the indenter's chemical and mechanical properties. In experiments, minimization of these effects requires special efforts in the measurement procedure (for example, calculation of the deformation of the indenter), whereas in simulations, we can easily exclude these effects—a virtual indenter represented by a repulsive potential force field depending on the distance to the conical surface independent of

the types of atoms it interacts with. The repulsive force acts only at distances smaller than $R_{\text{cut}} = 5 \text{ \AA}$ from the outer surface of the cone and is given by the expression

$$f = -k(R_{\text{cut}} - x) \quad (1)$$

where x is the distance from the atom to the outer surface of the cone and k is a constant parameter of the calculation procedure, which determines the strength of the repulsion. During preliminary tests, we found that the value $k = 0.5 \text{ eV}/\text{\AA}^2$ provides reasonable distances between the indenter and atoms of the studied sample. We keep this value the same for all calculations; however, it should be noted that a particular value of k was found not important.

2.2. Simulation Procedure. The most comprehensive simulation of nanoindentation is typically done with molecular dynamics, which allows taking into account the impact of temperature.^{21,47,48} However, such simulations are significantly time-consuming: it is necessary to simulate a system for milliseconds for correct relaxation, thermodynamic equilibration, and averaging. But even this time is not enough to describe the indenter penetration process at the experimental speed. Therefore, the penetration speed is artificially increased (to about ~ 10 to 100 m/s).^{21,47} In addition, an artificial thermostat cooling is often applied to the destruction zone.^{21,47} In this work, a description of the evolution of defects and obtaining the dependence of hardness on temperature is not critical, but excessive consumption of computational resources is highly undesirable. Therefore, the indentation process is simulated with the quasi-static approach that allows us to use the equilibration (energy minimization) procedure instead of time-consuming molecular dynamics. The depth of penetration of the indenter into the studied sample increases step by step in the course of hardness calculation by the same distance $\Delta = 0.5 \text{ \AA}$. At each step, full relaxation of all of the atoms of the studied sample is carried out (with the exception of the bottom atoms that are allowed to move only in the horizontal plane). The size of the periodic box (except the height) may also change to relax normal stresses on the side walls, whereas the position of the indenter during relaxation remains unchanged. For atomistic simulations, we have used the LAMMPS package.⁴⁹ Relaxation was performed by the conjugate gradient method.

At the end of each relaxation, the total force acting on the indenter is calculated. The absolute value of the z -component of this force, F_z , is precisely the load (with the opposite sign) that the material can withstand at the current penetration depth at zero temperature. Thus, as the result of simulation, we obtain the dependence of the load on the z -position of the indenter, which is then used to calculate nanohardness.

2.3. Nanohardness Calculation. The hardness of the material, measured at the macrolevel, is traditionally calculated as the ratio of the load (F_z) to the area of the formed imprint S_{imp} . This definition is useful at the macrolevel, where the dependence of the load on the depth of penetration (or imprint area) is almost linear, i.e., the hardness is almost independent of the depth of penetration and load. However, when measuring micro- and nanohardness, the dependence of the imprint area on the load is typically nonlinear, and the hardness is hence a function of the load rather than a single number.¹ Therefore, hardness, in its traditional definition, gives an averaged value over the current penetration depth. In addition to this quantity, we calculate and plot the “instantaneous” hardness defined as the derivative¹

$$H_{\text{inst}} = \partial F / \partial S_{\text{imp}} \quad (2)$$

The instantaneous hardness is more informative when analyzing the dependence of hardness on the penetration depth h .

As a rule, the actual penetration depth h does not coincide with the vertical travel of the tip due to compression of the material. To take into account a reversible elastic compression of the studied material, we calculate the averaged atom density in the 5 Å thick layer around the cone at the end of each relaxation step. Plotting this density as a function of vertical coordinate, we may find the position of the free surface as a density jump on this plot. The actual penetration depth h is calculated as the vertical distance between the position of the free surface and the position of the tip. Such an approach allows us to take into account the compression of the test sample near the indenter under load. Thus, the calculated actual penetration depth is used to find the contact area, $S_{\text{imp}} = \pi h^2$.

It should be noted that the described procedure allows for the calculation of hardness for various crystallographic orientations of the studied materials. This is of great importance for layered materials, where the hardness can vary significantly depending on the orientation of the crystal.

3. MLIP AND ACTIVE LEARNING

3.1. Moment Tensor Potentials. We used moment tensor potentials (MTPs)^{28,42} as a model of interatomic interaction. Similarly to the classical interatomic potentials, the energy E of an atomic configuration is partitioned into the sum of individual contributions (potentials) V_i of atoms: $E = \sum V_i$. MTPs implement many-body interaction; therefore, V_i depends on the type z_i of central atom i and also on the types $\{z_{i1}, \dots, z_{iK}\}$ and the relative positions $\{r_{i1}, \dots, r_{iK}\}$ of neighboring atoms within the cutoff radius R_{cut} .

The functional form of MTP is based on the representation of such atomic environments in the form of tensors $M_{\mu,\nu}$ of various ranks having the following form

$$M_{\mu,\nu}(z_i, \{z_{i1}, \dots, z_{iK}\}, \{r_{i1}, \dots, r_{iK}\}) = \sum_{1 \leq j \leq K} f_\mu(|r_{ij}|, z_i, z_j) \cdot u_{ij}^{\otimes \nu} \quad (3)$$

Here “ \otimes ” denotes the outer product; thus, $u_{ij}^{\otimes \nu}$ represents the tensor of inertia of rank ν of the atomic neighborhood. The first term $f_\mu(|r_{ij}|, z_i, z_j)$ in the right-hand side of eq 3 is the μ th radial function depending only on the distance $|r_{ij}|$ between atoms i and j and their types. We expand the radial functions through a set of radial basis functions $\varphi_\beta(|r_{ij}|)$ —Chebyshev polynomials—multiplied by $(R_{\text{cut}} - |r_{ij}|)^2$ for smoothing near the distances close to the cutoff radius

$$f_\mu(|r_{ij}|, z_i, z_j) = \varsigma_{\mu,z_i,z_j}^{(\beta)} \varphi_\beta(|r_{ij}|)(R_{\text{cut}} - |r_{ij}|)^2 \quad (4)$$

The coefficients of this expansion (radial coefficients) $\varsigma_{\mu,z_i,z_j}^{(\beta)} \varphi_\beta$ are found during the fitting.

Each contribution to the total energy V_i has the following form

$$V_i = \sum_{\alpha} \xi_{\alpha} B_{\alpha} \quad (5)$$

where ξ_{α} are the free parameters of the potential to be found while fitting and B_{α} are the basis functions constructed as contractions of the tensors $M_{\mu,\nu}$ to scalars. It can be shown⁴² that B_{α} are functions of atomistic neighborhoods invariant with

respect to orthogonal Euclidean transformations (rotations, reflections), as well as permutations of atoms of the same type.

The parameters of MTP $\theta = (\theta_1, \dots, \theta_n) = (\xi_{\alpha} \varsigma_{\mu,z_i,z_j}^{(\beta)})$ are found in the fitting (training) procedure by solving the minimization problem

$$\sum_k \left[w_e (E_k^{\text{DFT}} - E_k)^2 + w_f \sum_{l=1}^3 |f_{k,l}^{\text{DFT}} - f_{k,l}|^2 + w_s \sum_{l=1}^3 \sum_{m=1}^3 |\sigma_{k,l,m}^{\text{DFT}} - \sigma_{k,l,m}|^2 \right] \rightarrow \min \quad (6)$$

where E_k^{DFT} , $f_{k,l}^{\text{DFT}}$, and $\sigma_{k,l,m}^{\text{DFT}}$ are, respectively, the energy, atomic force components, and stress components calculated with the DFT for the k th configuration from the training set, and w_e , w_f and w_s are non-negative weights expressing the relative importance of energies, forces, and stresses in the optimization, respectively. Since the functional form of the MTP potentials depends on the parameters in a nonlinear way, the procedure for training them is based on nonlinear optimization using a quasi-Newton method of the second order.

For each compound, we trained an MTP that was used to calculate the hardness along all of the crystallographic directions. All of these MTPs have the same number of coefficients ξ_{α} equal to 288. The total number of parameters θ was between 310 and 470 depending on the number of species (the more, the larger).

3.2. Active Learning. The construction of an optimal training set is not a trivial task, and we do it during the simulation. In our previous works,^{29,32,46} we have applied active learning to train an MLIP on the fly. Active learning allows detecting configurations that trigger extrapolation when MLIP calculates the energy. If such an “extrapolative” configuration is detected, it is added to the training set (with the energy and forces calculated with DFT), and the MLIP is retrained.

The mechanism of extrapolation detection is based on the D-optimality criterion,⁵⁰ assuming that the training set must contain n “extreme” configurations $\text{cfg}_1, \dots, \text{cfg}_n$ maximizing the modulus of determinant of the linearized design matrix

$$A = \begin{pmatrix} \frac{\partial E(\text{cfg}_1)}{\partial \theta_1} & \dots & \frac{\partial E(\text{cfg}_1)}{\partial \theta_n} \\ \vdots & \ddots & \vdots \\ \frac{\partial E(\text{cfg}_n)}{\partial \theta_1} & \dots & \frac{\partial E(\text{cfg}_n)}{\partial \theta_n} \end{pmatrix} \quad (7)$$

among all relevant configurations. We say that MLIP extrapolates on some configuration cfg_* if this requirement is violated, i.e., if swapping some row in A by a vector $b^T = \left(\frac{\partial E(\text{cfg}_*)}{\partial \theta_1} \dots \frac{\partial E(\text{cfg}_*)}{\partial \theta_n} \right)$ leads to an increase of $|\det A|$. In practice, to detect extrapolation⁴⁶ on the configuration cfg_* , one needs to calculate the extrapolation grade

$$\gamma = \max |b \cdot A^{-1}| \quad (8)$$

indicating the maximal possible factor by which $|\det A|$ can increase if one of the rows of A is replaced by b^T . Thus, if $\gamma \leq 1$, MLIP interpolates on the configuration cfg_* and extrapolates otherwise.

However, this active learning method cannot be applied to train MLIP on the fly during nanohardness calculations.⁵¹ In the context of this application, we deal with configurations

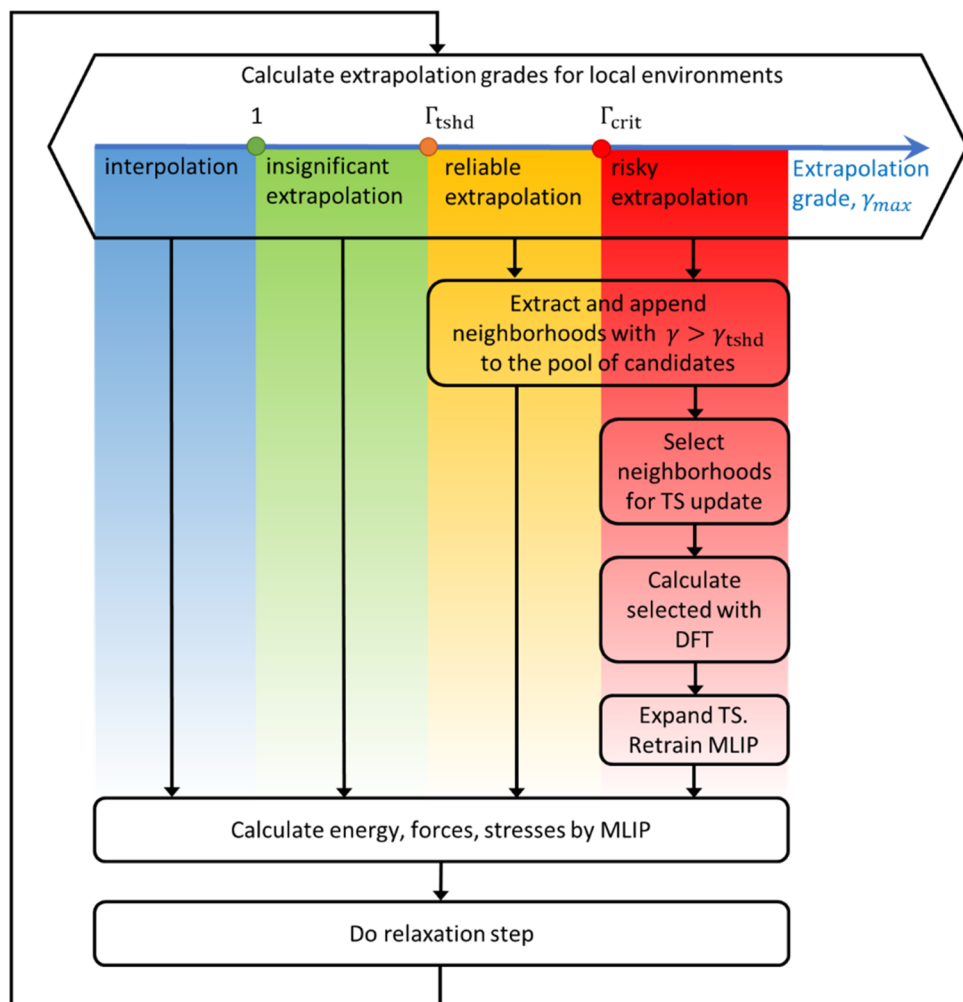


Figure 2. Scheme of the learning on-the-fly workflow. The extrapolation grade is calculated for each atomic neighborhood. If the highest extrapolation grade is beyond the critical value, the MLIP is retrained.

containing tens of thousands of atoms. Therefore, large configurations cannot be treated with DFT, which makes such learning on-the-fly approach inapplicable. Additionally, the described method for the extrapolation detection may erroneously ignore a large configuration with some local “extrapolative” arrangement of atoms in a small subdomain (since it is effectively average, the extrapolation grade over all atoms). In this paper, the active learning methodology was adapted for detecting extrapolation on local atomistic environments. This methodology is suitable for active learning on the fly when treating large configurations.

According to the suggested method, the linearized matrix A , in this case, consists of the derivatives of site energies V_1, \dots, V_n of the atomistic neighborhoods

$$A = \begin{pmatrix} \frac{\partial V_1}{\partial \theta_1} & \dots & \frac{\partial V_1}{\partial \theta_n} \\ \vdots & \ddots & \vdots \\ \frac{\partial V_n}{\partial \theta_1} & \dots & \frac{\partial V_n}{\partial \theta_n} \end{pmatrix} \quad (9)$$

Since the site energy depends only on the atomic positions and types within the cutoff sphere, maximization of $|\det A|$ (D-optimality criterion) can be interpreted as selecting the most

“extreme” atomic neighborhoods, in contrast to the selection of entire configurations in the more traditional approach described above. Note that the selected neighborhoods may belong to different configurations.

The selection criterion defines the extrapolation detection method. Thus, the extrapolation grade of the neighborhood is defined as $\gamma = \max |b \cdot A^{-1}|$, $b = \left(\frac{\partial V_1}{\partial \theta_1}, \dots, \frac{\partial V_n}{\partial \theta_n} \right)$ and is calculated for each atom in a configuration. If $\gamma \geq 1$, it is interpreted as extrapolation while calculating the site energy and interpolation otherwise (note that in the previous method, we detected extrapolation while calculating the energy of the configuration).

The atomic neighborhoods typically contain up to 150 atoms, which is suitable for DFT calculations. Thus, the extrapolative neighborhoods are treated as configurations with no periodicity (as an atomic cluster) in the course of DFT calculations. This “forces” the MTP to learn the behavior of the surface atoms. However, it does not lead to learning of the irrelevant information since free surfaces are anyway present in the simulation and need to be learned. At the same time, the application of this technique to materials with strong surface effects requires the treatment of relatively large neighborhoods with several hundreds or even thousands of atoms that may be problematic for DFT calculations.

It is important to note here that MLIP assumes that the site energy does not depend on anything beyond the cutoff sphere (locality assumption). Therefore, the cutoff radius must be carefully chosen to take into account the fact that the interatomic interaction at the surface is less local. In our calculations, we choose the cutoff radius larger than in empirical potentials.

It is important to note the difference in the cluster size in our method and in the MD-QM coupling approach (see, for example, ref 52). In the MD-QM coupling approach, atomic clusters are built for the calculation of the forces with DFT. If we admit the assumption of the locality of interatomic interaction, MD-QM requires a two times larger atomic clusters compared to our approach to account for interactions between atoms of the same distance. Indeed, the site energy of local potential depends on atomic positions within the cutoff sphere, while forces depend on the positions of atoms within a sphere of the double cutoff radius.

In this work, we used density functional theory implemented in the Vienna Ab initio Simulation Package (VASP)⁵³ with Generalized Gradient Approximation (GGA) and the projector augmented wave (PAW) method^{54,55} within the Perdew–Burke–Ernzerhof (PBE)⁵⁶ exchange–correlation functional to fit MTPs. Gaussian smearing with a width of 0.03 eV was used in all DFT calculations.

To minimize the interaction of the atomic cluster with itself through the periodic boundaries, the supercell was constructed with orthogonal lattice vectors with a length equal to cluster diameter plus 15 Å. These calculations were done on a single k -point grid.

3.3. Learning On-the-Fly Algorithm. Learning the on-the-fly procedure used in this work is formalized in the following steps:

1. We start from an MTP trained on some training set (consisting of small equilibrated configurations with and without free surfaces) and the initial matrix A , whose rows correspond to the local neighborhoods of configurations from the training set.

2. At each step of the nanohardness calculation procedure, we run relaxation. At each relaxation step, the extrapolation grade

$$\gamma_s = \max |b_s \cdot A^{-1}|, \quad b_s = \left(\frac{\partial V_s}{\partial \theta_1}, \dots, \frac{\partial V_s}{\partial \theta_n} \right)$$

is calculated and is maximized over all of the atoms, $\gamma_{\max} = \max_s \gamma_s$ prior to calculation of site energies, V_s . Further steps depend on the degree of extrapolation (see the scheme in Figure 2).

2.1. If $\gamma_{\max} \leq 1$ (interpolation) or $1 < \gamma_{\max} \leq \Gamma_{\text{tshd}} = 2$ (insignificant extrapolation), we proceed to step 2.

2.2. $\gamma_{\max} \geq 2$, all of the extrapolative atomistic neighborhoods (with $\gamma_s > 2$) are appended to the pool of candidates for training.

2.2.1. If $\gamma_{\max} < \Gamma_{\text{crit}} = 10$, the extrapolation is acceptable, and we proceed to step 2.

2.2.2. If the degree of extrapolation on some atomistic neighborhoods is larger than a critical value ($\gamma_{\max} \geq \Gamma_{\text{crit}} = 10$), the risk to obtain forces or stresses with significant error is high, which may lead to relaxation failure. Therefore, relaxation is interrupted to update the MLIP. Thus, the atomistic simulation continues either until successful completion or until it stops with a too high extrapolation grade ($\gamma_{\max} > \Gamma_{\text{crit}} = 10$).

2.2.2.1. At this step, we select the atomistic neighborhoods for learning from all sampled extrapolative neighborhoods. This is equivalent to finding the design matrix A with maximal $|\det A|$. Thus, row-vectors b_s are calculated for each of the extrapolative neighborhoods and for the neighborhoods of configurations from the training set. Next, we choose among these vectors those that maximize $|\det A|$ using the computationally efficient Maxvol algorithm.⁵⁷ Note that topologically similar neighborhoods are automatically discarded during this procedure. Typically, a few dozens of atomistic neighborhoods are selected for learning among many thousands of candidates.

2.2.2.2. The energies, forces, and stresses are calculated for the newly selected (i.e., not already present in the training set) neighborhoods with DFT.

2.2.2.3. The selected neighborhoods with the calculated DFT data are appended to the training set, and then the MLIP is retrained.

Step 3. The energy, forces on atoms, and stresses are calculated with the MTP at the current relaxation step.

Step 4. The calculated energy, forces, and stresses are used to find the displacements of atoms at the next relaxation step according to the relaxation method (conjugate gradient method in our case). The procedure repeats from step 1.

4. RESULTS AND DISCUSSION

4.1. Scope of Simulation. With the proposed methodology, we have simulated indentation and calculated nanohardness of several compounds with one, two, and three types of atoms: diamond, silicon carbide (3C and 4H polytypes), aluminum nitride, heterodiamond BC₂N, and silicon. Each material was indented in a number of different orientations to demonstrate the impact of anisotropy. As a result of simulations, we have obtained nanohardness as a function of the penetration depth. Our calculation results were validated against the data from the literature and our experiment.

In the course of preliminary simulations, we have varied the size of the studied material and analyzed the impact of the finite domain size on the results. We found that the domain size of 10 nm yields the results converged to within 5% for all of the materials. Therefore, in all calculations, the studied material had a cubic shape with a side of about 10 nm. The maximal depth of penetration was 3.5 nm.

For each compound, the training procedure started from the periodic structure relaxed with DFT (only one in the initial training set), serving as an initial training set for MTP. When such MTP is being applied for relaxation, the active learning algorithm detects extrapolation on the free surface. In this way, the MLIP automatically learns those extrapolative neighborhoods. Next, the sample of studied material slightly compresses on the first several iterations of relaxation due to surface effects and atoms on the surface start reconstructing. This process is accompanied by intensive learning of new atomic neighborhoods. Intensive learning also continues at the beginning of the penetration stage, when an imprint is being formed in the sample of material. On later steps of relaxation, the frequency of simulation interruptions to retrain the potential is getting low,

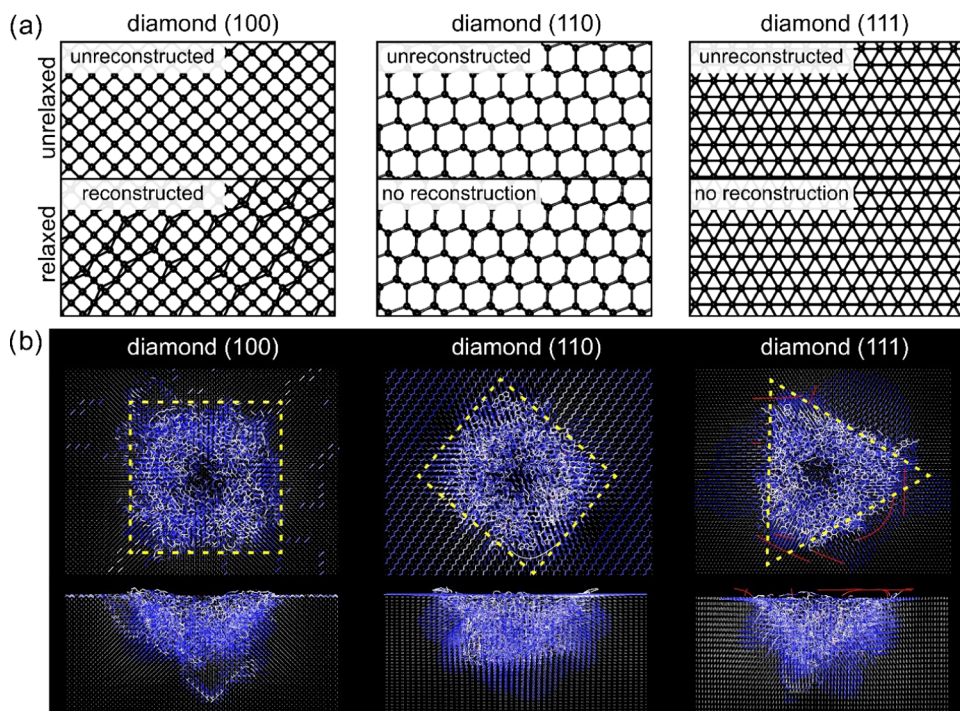


Figure 3. (a) Top view of the unrelaxed and relaxed structure of different surfaces of diamond. Only the (100) surface of diamond has a reconstructed surface after relaxation. (b) Top and side views of crystal structures of indented surfaces of diamond with (100), (110), and (111) crystallographic orientations at the load of $3.5 \mu\text{N}$. Bonds are colored according to their length. The blue color corresponds to 1.45 \AA , while the red color is 1.25 \AA .

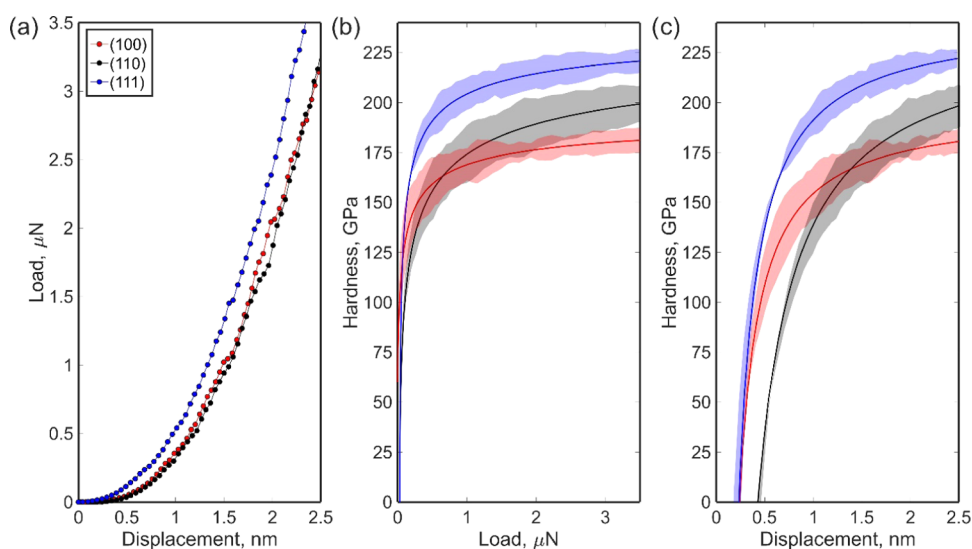


Figure 4. (a) Load–depth curves for the diamond surfaces. Dependence of nanohardness, H_{inst} on (b) applied load and (c) displacement. Red, black, and blue colors refer to (100), (110), and (111) surfaces, respectively. Shadow areas in (b, c) represent uncertainty in the calculated hardness related to the difference between numerical data of load–displacement curve and its analytical fit by a quadratic function.

while the number of sampled neighborhoods (candidates for selection) after each simulation interruption is growing.

The cutoff radius for C, SiC, and BC₂N was 5 Å, 6 Å for AlN, and 8 Å for Si. The total number of DFT calculations (equal to the number of configurations in the training set) was

- 617 for diamond,
- 959 for silicon carbide (both allotropes),
- 897 for aluminum nitride,
- 1606 for BC₂N,
- 607 for silicon.

The number of atoms in the course of the simulations was about 185 000, 100 000, 100 000, and 160 000 for these compounds, respectively. Most of the computational time (about 70%) was spent on DFT calculations. About 2% of the total computational time was spent on fitting the potential and selection of the neighborhoods for calculation on DFT. The rest of the time was spent on the atomistic simulation of indentation.

The hardness of the materials under consideration reported in the literature is measured on a macro- or microlevel. Therefore, a quantitative comparison of the calculated nanohardness with the available experimental results is not possible. In addition,

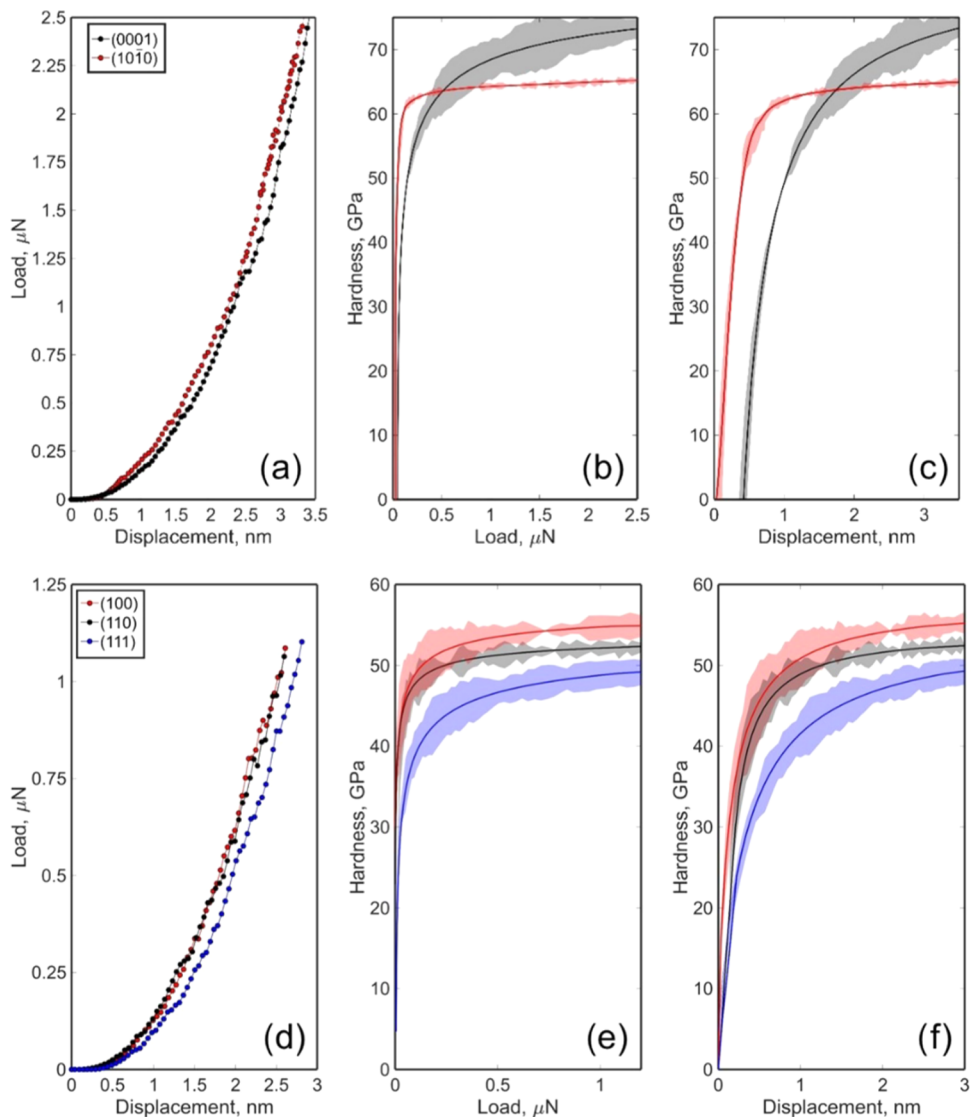


Figure 5. Calculated data for 4H-SiC: (a) load–depth curves; dependence of nanohardness, H_{inst} , on (b) load and (c) indentation depth. Calculated data for 3H-SiC: (d) load–depth curves; dependence of hardness on (e) load and (f) indentation depth.

experimental data for some materials are provided without specification of the crystallographic direction of measurement. It motivated us to carry out experimental measurements of nanohardness for silicon films to verify the calculation results. The results of comparison and details of the experiment are reported in the *Supporting Information*.

4.2. Diamond. For diamond, we calculated hardness along the three main crystallographic planes, which are usually obtained in experiments, namely, (100), (110), and (111); see Figure 3a. Only the (100) surface of diamond has a reconstructed surface after relaxation, which agrees well with previous findings.^{58,59} The structures with the indentation depth of ~3 nm are shown in Figure 3b. It is clearly seen that the shape of an imprint is determined by the symmetry of the surface. For the (111) surface (Figure 3b), where the threefold symmetry axis exists, the imprint has a triangular shape, while for other surfaces, the square-like shape is observed (Figure 3b). In Figure 3b, the calculated dependencies of the load on the indentation depth are shown for the three considered diamond surfaces.

It is known from experiments that the highest value of hardness belongs to the (111) surface.^{17,60,61} There is recent

theoretical work²³ where the hardness was calculated by the simulation of nanoindentation using a modified Tersoff potential. These results show the nanohardness of a diamond equals 212, 227, and 225 GPa for the (100), (110), and (111) surfaces, respectively.²³ The ratio of these values is in good agreement with our results (see Figure 4) in which the hardness calculated at the maximum applied load (3.5 μN) for these surfaces was found to be 180, 198, and 220 GPa, respectively. We have also compared this ratio to the experimental data from ref 18. The hardness reported in ref 18 is 175 GPa for the (111) surface and 150 GPa for the (100) surface. Both in the experiment and in our calculations (Figure 4), the hardness of the facet (111) is 1.2 times higher than the hardness of the facet (100). The same trend was observed for diamond films with (100) and (111) surfaces measured by sclerometry.⁶² Empirical models provide orientationally average hardness ~95 GPa (Vickers hardness by the Mazhnik–Oganov model¹⁶). It should be noted that all of the empirical models are based on experimental values of macro- or microhardness. However, they provide a lower bound for nanohardness.

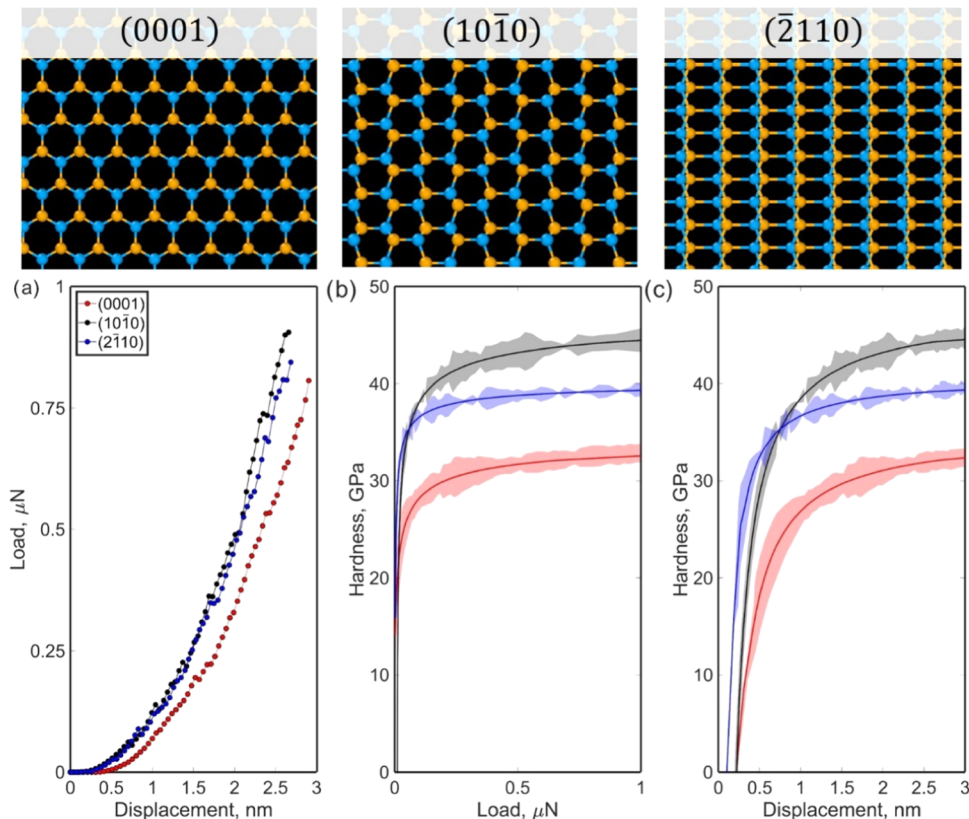


Figure 6. (a) Load–depth curves; dependence of nanohardness, H_{inst} , on (b) load and (c) indentation depth for two orientations of AlN. Red, black, and blue colors refer to (0001), (10\bar{1}0), and (\bar{2}110) surfaces, respectively. Shadow areas in the (b, c) represent errors in the calculated hardness.

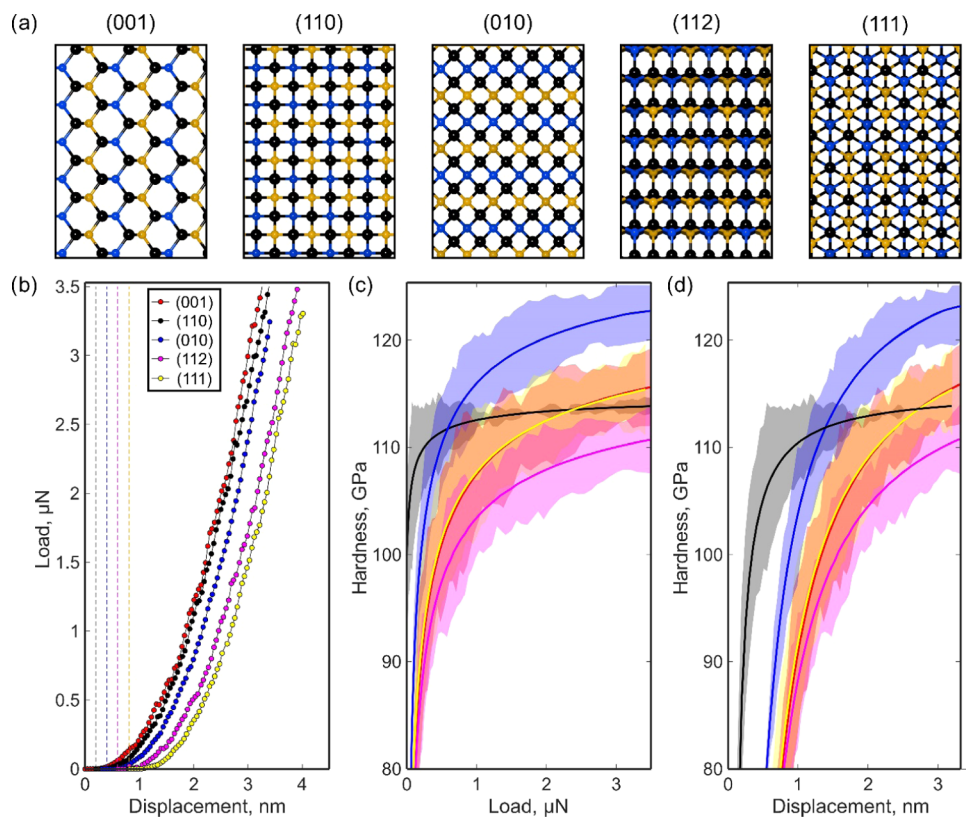


Figure 7. (a) Top views of the considered surfaces of cubic BC₂N; blue balls are boron atoms; black is carbon; orange is nitrogen. (b) Load–depth curves; dependence of nanohardness on (c) load and (d) indentation depth for all of the considered orientations of cubic BC₂N. Dashed vertical lines represent shifts of each curve along the x -axis for clarity of visualization. Shadowed areas in the (c, d) represent errors in the calculated hardness.

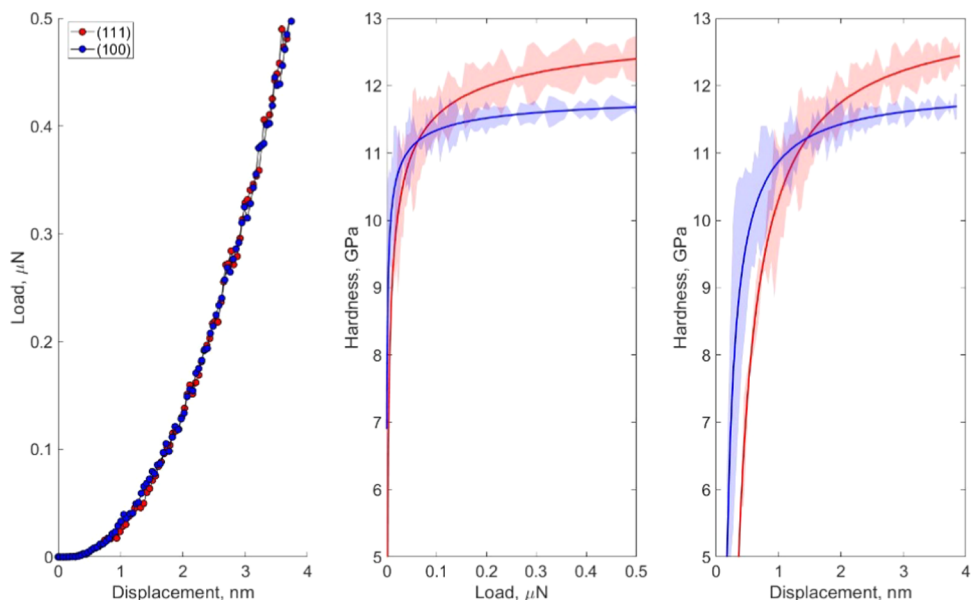


Figure 8. Load–displacement curves for silicon and the dependencies of nanohardness, H_{inst} , on the load and indentation depth for the (100) and (111) orientations of Si.

4.3. Silicon Carbide. The next material exhibiting anisotropy of hardness is silicon carbide. As these compounds usually display a wide variety of stable low-energy polytypes, we chose two of the most widespread, namely, 3C and 4H.

For 4H-SiC, we simulated nanoindentation for the (0001) and (10 $\bar{1}$ 0) crystallographic planes, whereas for 3C-SiC, we chose the same crystallographic planes as for diamond (namely, (100), (110), and (111)). The calculated dependencies of nanohardness H_{inst} on the load for the various crystallographic orientations of 4H and 3C-SiC polytypes are shown in Figure 5b,e. It is noteworthy that the nanohardness of the (0001) plane of 4H polytype is higher than that of the (10 $\bar{1}$ 0) plane. The obtained values of hardness for maximum simulated load for 4H-SiC were found to be 72 and 64 GPa (for the (0001) and (10 $\bar{1}$ 0) surfaces, respectively).

The experimentally measured Vickers hardness⁶³ of 4H-SiC at the load of 20 mN equal to 40 and 38 GPa for the (0001) and (10 $\bar{1}$ 0) surfaces. In the case of 3C-SiC, reliable experimental measurements were made for the (111) oriented thin 3C-SiC films⁶⁴ for the loads from 5 to 50 mN. Vickers hardness, in this case, varied from 25 to 30 GPa, while our approach gives the nanohardness of the (100), (110), and (111) crystallographic planes of 3C-SiC at maximal loads as 54, 52, and 49 GPa, respectively. Empirical models of hardness estimate the (macro-)hardness of 3C-SiC as 31–35 GPa, while for 4H-SiC, it is 28–32 GPa.

4.4. Aluminum Nitride. Here, we performed the calculations for three crystallographic orientations, namely, (0001), (10 $\bar{1}$ 0), and (2110). Figure 6 shows the dependencies of load on the actual indentation depth and the dependence of calculated nanohardness H_{inst} on the load and actual indentation depth for AlN. Load–depth curves show that the highest nanohardness is devoted to the (10 $\bar{1}$ 0) surface (black line in Figure 6a). Calculated dependences of hardness on the load and indentation depth clearly show that the critical values of nanohardness obey the following order: $H_{\text{inst}}(10\bar{1}0) > H_{\text{inst}}(\bar{2}110) > H_{\text{inst}}(0001)$ (Figure 6b,c). It should be noted that the behavior of hardness (Berkovitch hardness) on the displacement was observed in the experimental study of AlN by Jian et al.⁶⁵ The measured

dependence of Berkovitch hardness on the penetration depth shows a nonlinear behavior with the maximum value of hardness of 40 GPa achieved for the depth of ~11 nm. An increase in applied load (indentation depth < 11 nm) led to a reduction of hardness, approaching a plateau with a value of 22 GPa.⁶⁵ The same behavior of hardness, depending on the penetration depth, was also observed for superhard higher tungsten boride phases.⁶⁶ Such behavior can be revealed only at small values of applied load ~1 μ N, as was used in our case.

4.5. Heterodiamond BC₂N. Simulation of the nanoindentation of superhard heterodiamond BC₂N demonstrates the applicability of our method to ternary materials. The experimental measurements reported the Vickers hardness of about 76 GPa,^{67,68} which agrees well with estimations by the empirical Mazhnik–Oganov model (73 GPa). We defined five crystallographic orientations of cubic BC₂N, for which the nanoindentation process was simulated. The obtained load–depth curves together with dependencies of nanohardness on depth and load are shown in Figure 7. Unfortunately, the calculated hardness anisotropy in BC₂N cannot be compared with the experimental results due to the absence of orientation-dependent data.

4.6. Silicon. Calculated indentation curves for silicon (100) and (111) surfaces are shown in Figure 8. The maximum hardness is devoted to the (111) surface of silicon and equal to 12.5 GPa, while for the (100) surface, the maximum hardness is 11.7 GPa. The experimental value of Vickers hardness of silicon is 11.1 GPa.⁶⁹ Berkovitch indentation on a (111) surface gives values from 12 to 14 GPa.^{70,71} Empirical Mazhnik–Oganov model¹⁶ gives the value of 7.7 GPa for silicon, which is lower than our experimental and computational data.

4.7. Discussion. The available experimental data on hardness for the materials under consideration were obtained at macro- and microlevels. The calculated hardness at the nanolevel is systematically higher (typically, 1.2–1.5 times) than the measured one. Orientationally averaged values of (macro-)hardness calculated with the empirical Mazhnik–Oganov model¹⁶ (as well as for other empirical models^{12–15}) are close to the experimental data (used to fit it) and also give

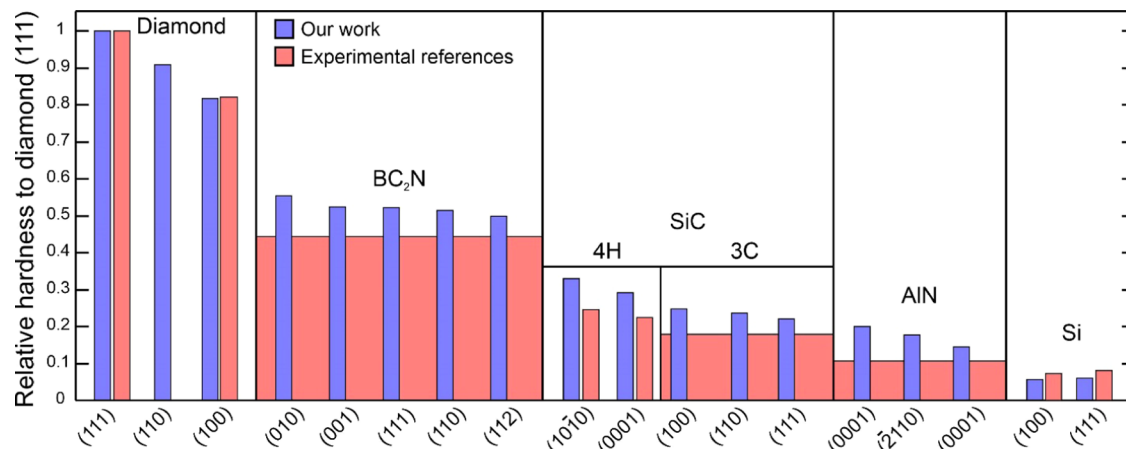


Figure 9. Comparison of the calculated (blue bars) and experimental (red bars) relative hardness of the considered compounds normalized on the hardest diamond (111) surface. For those materials which have no anisotropic data, the one value is shown by a wide bar.

underestimated values compared to our data for all of the studied materials. To perform a consistent comparison with our results, we calculated the relative values, normalized to the hardness of diamond along the (111) crystallographic plane (the experimental data were normalized on the measured hardness, whereas the calculated nanohardness was normalized on the calculated nanohardness of the diamond). The results of the comparison of the relative hardness are shown in Figure 9. The obtained data on the relative hardness clearly reveal a correlation between the calculated data and experimental values in the space of the compounds under consideration. This indicates the reliability of our approach to calculating the material's nanohardness via nanoindentation simulations.

5. CONCLUSIONS

The application of machine learning in material science enables solving many problems that were out of reach for the traditional methods. In our work, machine learning is applied to learn the behavior of the first-principles model and reproduce it in the classical atomistic simulation of nanoindentation modeling. The core of the proposed method is an active learning algorithm enabling automatic construction of the training set and ensuring the reliability of simulations. The designed active learning algorithm can detect new (unlearned) atomistic environments and learn them, systematically synchronizing the training and simulation domains in the configurational space. For the first time, we demonstrate automatic training of a machine-learning potential applied to simulations of such complexity.

In contrast to empirical potentials traditionally used for this class of problems, in our approach, machine-learning potentials are an intermediate tool used to approximate DFT with a flexible, systematically refinable functional form. This makes our approach suitable for high-throughput searches for novel materials, as it does not require the tedious stage of manually developing a potential for each of the candidate materials; on the contrary, the potential is being created in the course of simulation "from scratch". In contrast to empirical models such as the Chen model,¹⁵ the proposed methodology is suitable for predicting nanohardness (as opposed to macrohardness to which the corresponding empirical models are fitted), takes into account anisotropy, does not suffer from transferability issues, and is capable of reconstructing the entire hardness versus penetration depth dependence.

ASSOCIATED CONTENT

Supporting Information

The Supporting Information is available free of charge at <https://pubs.acs.org/doi/10.1021/acs.jctc.1c00783>.

Details of experimental hardness measurements for silicon and a comparison of the calculated and measured results (S1) ([PDF](#))

AUTHOR INFORMATION

Corresponding Author

Evgeny V. Podryabinkin – Skolkovo Institute of Science and Technology, Moscow 121025, Russia; [orcid.org/0000-0001-9057-7249](#); Email: e.podryabinkin@skoltech.ru

Authors

Alexander G. Kvashnin – Skolkovo Institute of Science and Technology, Moscow 121025, Russia; [orcid.org/0000-0002-0718-6691](#)

Milad Asgarpour – Skolkovo Institute of Science and Technology, Moscow 121025, Russia; University of Limerick, Limerick V94 T9PX, Ireland

Igor I. Maslenikov – Technological Institute of Superhard and Novel Carbon Materials, Moscow 108840, Russia

Danila A. Ovsyannikov – Technological Institute of Superhard and Novel Carbon Materials, Moscow 108840, Russia

Pavel B. Sorokin – Technological Institute of Superhard and Novel Carbon Materials, Moscow 108840, Russia; National University of Science and Technology "MISiS", Moscow 119049, Russia; [orcid.org/0000-0001-5248-1799](#)

Mikhail Yu Popov – Technological Institute of Superhard and Novel Carbon Materials, Moscow 108840, Russia; National University of Science and Technology "MISiS", Moscow 119049, Russia

Alexander V. Shapeev – Skolkovo Institute of Science and Technology, Moscow 121025, Russia

Complete contact information is available at:

<https://pubs.acs.org/10.1021/acs.jctc.1c00783>

Author Contributions

E.V.P., A.G.K., and A.V.S. conceived this project. I.I.M., D.A.O., and M.Y.P. performed the experiments and analyzed obtained data. E.V.P. and A.G.K. prepared the theoretical calculations and analysis. E.V.P., A.G.K., M.Y.P., and A.V.S. wrote and revised the

paper. All of the authors discussed the results and offered useful inputs.

Notes

The authors declare no competing financial interest. The source code of the MLIP package implementing MTPs used in this paper can be requested under a general academic license by following the general instructions at [<https://mlip.skoltech.ru/download/>] and pulling the “hardness” branch of the code. The datasets generated and analyzed during the current study including: the trained on-the-fly machine-learning potentials (and the corresponded training sets), snapshots of atomistic simulation (LAMMPS dump files), data required for construction of the force versus depth curves are available at [<https://drive.google.com/file/d/1OqRagPOqMqWtiNhEeEuRwAILaLvpFNm1/view?usp=sharing>] repository. LAMMPS scripts for simulation of nanoindentation and scripts used for the automation of the learning on-the-fly routines are available at [<https://drive.google.com/file/d/1NS9-wRAOKDEATxumopp1elUHNEqqKAqr/view?usp=sharing>] repository.

ACKNOWLEDGMENTS

E.V.P. and A.V.S. acknowledge financial support from the Russian Science Foundation (grant no. 18-13-00479) for the development of machine-learning interatomic potentials and for the development of active learning of local atomic environments. A.G.K., I.I.M., and M.Y.P. acknowledge financial support from the Russian Science Foundation (grant no. 20-12-00097) for calculations of nanohardness and experimental measurements. M.Y.P. acknowledges the support of the Ministry of Science and Higher Education of the Russian Federation in the framework of the State Task (project code 0718-2020-0037) for discussion of obtained results.

REFERENCES

- (1) Broitman, E. Indentation Hardness Measurements at Macro-, Micro-, and Nanoscale: A Critical Overview. *Tribol. Lett.* **2017**, *65*, No. 23.
- (2) Brinell, J. A. Way of Determining the Hardness of Bodies and Some Applications of the Same. *Tek. Tidskr.* **1900**, *5*, 69–87.
- (3) Smith, R. L.; Sandly, G. E. An Accurate Method of Determining the Hardness of Metals, with Particular Reference to Those of a High Degree of Hardness. *Proc. Inst. Mech. Eng.* **1922**, *102*, 623–641.
- (4) Fischer-Cripps, A. C. Analysis of Nanoindentation Test Data. In *Nanoindentation*; Springer: New York, NY, 2011; pp 39–75.
- (5) Broitman, E. The Nature of the Frictional Force at the Macro-, Micro-, and Nano-Scales. *Friction* **2014**, *2*, 40–46.
- (6) Eriksson, R.; Gupta, M.; Broitman, E.; Jonnalagadda, K. P.; Nylén, P.; Lin Peng, R. Stresses and Cracking During Chromia-Spinel-NiO Cluster Formation in TBC Systems. *J. Therm. Spray Technol.* **2015**, *24*, 1002–1014.
- (7) Huang, Y.; Zhang, F.; Hwang, K. C.; Nix, W. D.; Pharr, G. M.; Feng, G. A Model of Size Effects in Nano-Indentation. *J. Mech. Phys. Solids* **2006**, *54*, 1668–1686.
- (8) Chen, J.; Bull, S. J. On the Factors Affecting the Critical Indenter Penetration for Measurement of Coating Hardness. *Vacuum* **2009**, *83*, 911–920.
- (9) Bückle, H. Progress in Micro-Indentation Hardness Testing. *Metall. Rev.* **1959**, *4*, 49–100.
- (10) Korsunsky, A. M.; McGurk, M. R.; Bull, S. J.; Page, T. F. On the Hardness of Coated Systems. *Surf. Coat. Technol.* **1998**, *99*, 171–183.
- (11) Fischer-Cripps, A. C. Critical Review of Analysis and Interpretation of Nanoindentation Test Data. *Surf. Coat. Technol.* **2006**, *200*, 4153–4165.
- (12) Gao, F. Theoretical Model of Intrinsic Hardness. *Phys. Rev. B* **2006**, *73*, No. 132104.
- (13) Simánek, A.; Vackar, J. Hardness of Covalent and Ionic Crystals: First-Principle Calculations. *Phys. Rev. Lett.* **2006**, *96*, 85501–85505.
- (14) Lyakhov, A. O.; Oganov, A. R. Evolutionary Search for Novel Superhard Materials: Methodology and Applications to Forms of Carbon and TiO₂. *Phys. Rev. B* **2011**, *84*, No. 092103.
- (15) Chen, X.-Q.; Niu, H.; Li, D.; Li, Y. Modeling Hardness of Polycrystalline Materials and Bulk Metallic Glasses. *Intermetallics* **2011**, *19*, 1275–1281.
- (16) Mazhnik, E.; Oganov, A. R. A Model of Hardness and Fracture Toughness of Solids. *J. Appl. Phys.* **2019**, *126*, No. 125109.
- (17) Kraus, E. H.; Slawson, C. B. Variation of Hardness in the Diamond. *Am. Mineral.* **1939**, *24*, 661–676.
- (18) Blank, V.; Popov, M.; Pivovarov, G.; Lvova, N.; Terentev, S. Mechanical Properties of Different Types of Diamond. *Diamond Relat. Mater.* **1999**, *8*, 1531–1535.
- (19) Yeo, S.; Yun, J.; Kim, S.; Cho, M. S.; Lee, Y.-W. Fabrication Methods and Anisotropic Properties of Graphite Matrix Compacts for Use in HTGR. *J. Nucl. Mater.* **2018**, *499*, 383–393.
- (20) Ma, Z. S.; Zhou, Y. C.; Long, S. G.; Lu, C. On the Intrinsic Hardness of a Metallic Film/Substrate System: Indentation Size and Substrate Effects. *Int. J. Plast.* **2012**, *34*, 1–11.
- (21) Fu, T.; Peng, X.; Chen, X.; Weng, S.; Hu, N.; Li, Q.; Wang, Z. Molecular Dynamics Simulation of Nanoindentation on Cu/Ni Nanotwinned Multilayer Films Using a Spherical Indenter. *Sci. Rep.* **2016**, *6*, No. 35665.
- (22) Verkhovtsev, A. V.; Yakubovich, A. V.; Sushko, G. B.; Hanuske, M.; Solov'yov, A. V. Molecular Dynamics Simulations of the Nanoindentation Process of Titanium Crystal. *Comput. Mater. Sci.* **2013**, *76*, 20–26.
- (23) Huang, C.; Peng, X.; Yang, B.; Xiang, H.; Sun, S.; Chen, X.; Li, Q.; Yin, D.; Fu, T. Anisotropy Effects in Diamond under Nanoindentation. *Carbon* **2018**, *132*, 606–615.
- (24) Du, X.; Zhao, H.; Zhang, L.; Yang, Y.; Xu, H.; Fu, H.; Li, L. Molecular Dynamics Investigations of Mechanical Behaviours in Monocrystalline Silicon Due to Nanoindentation at Cryogenic Temperatures and Room Temperature. *Sci. Rep.* **2015**, *5*, No. 16275.
- (25) Ruestes, C. J.; Bringa, E. M.; Gao, Y.; Urbassek, H. M. Molecular Dynamics Modeling of Nanoindentation. In *Applied Nanoindentation in Advanced Materials*; John Wiley & Sons, Ltd., 2017; pp 313–345.
- (26) Bernstein, N.; Csányi, G.; Deringer, V. L. De Novo Exploration and Self-Guided Learning of Potential-Energy Surfaces. *npj Comput. Mater.* **2019**, *5*, No. 99.
- (27) Ouyang, R.; Xie, Y.; Jiang, D. Global Minimization of Gold Clusters by Combining Neural Network Potentials and the Basin-Hopping Method. *Nanoscale* **2015**, *7*, 14817–14821.
- (28) Gubaev, K.; Podryabinkin, E. V.; Hart, G. L. W.; Shapeev, A. V. Accelerating High-Throughput Searches for New Alloys with Active Learning of Interatomic Potentials. *Comput. Mater. Sci.* **2019**, *156*, 148–156.
- (29) Podryabinkin, E. V.; Tikhonov, E. V.; Shapeev, A. V.; Oganov, A. R. Accelerating Crystal Structure Prediction by Machine-Learning Interatomic Potentials with Active Learning. *Phys. Rev. B* **2019**, *99*, No. 064114.
- (30) Xia, K.; Gao, H.; Liu, C.; Yuan, J.; Sun, J.; Wang, H.-T.; Xing, D. A Novel Superhard Tungsten Nitride Predicted by Machine-Learning Accelerated Crystal Structure Search. *Sci. Bull.* **2018**, *63*, 817–824.
- (31) Deringer, V. L.; Proserpio, D. M.; Csányi, G.; Pickard, C. J. Data-Driven Learning and Prediction of Inorganic Crystal Structures. *Faraday Discuss.* **2018**, *211*, 45–59.
- (32) Novikov, I. S.; Shapeev, A. V.; Suleimanov, Y. V. Ring Polymer Molecular Dynamics and Active Learning of Moment Tensor Potential for Gas-Phase Barrierless Reactions: Application to S + H₂. *J. Chem. Phys.* **2019**, *151*, No. 224105.
- (33) Artrith, N.; Urban, A.; Ceder, G. Constructing First-Principles Phase Diagrams of Amorphous Li x Si Using Machine-Learning-Assisted Sampling with an Evolutionary Algorithm. *J. Chem. Phys.* **2018**, *148*, No. 241711.

- (34) Sosso, G. C.; Miceli, G.; Caravati, S.; Behler, J.; Bernasconi, M. Neural Network Interatomic Potential for the Phase Change Material GeTe. *Phys. Rev. B* **2012**, *85*, No. 174103.
- (35) Rossi, K.; Pártay, L. B.; Csányi, G.; Baletto, F. Thermodynamics of CuPt Nanoalloys. *Sci. Rep.* **2018**, *8*, No. 9150.
- (36) Kobayashi, R.; Giofré, D.; Junge, T.; Ceriotti, M.; Curtin, W. A. Neural Network Potential for Al-Mg-Si Alloys. *Phys. Rev. Mater.* **2017**, *1*, No. 053604.
- (37) Litman, Y.; Behler, J.; Rossi, M. Temperature Dependence of the Vibrational Spectrum of Porphycene: A Qualitative Failure of Classical-Nuclei Molecular Dynamics. *Faraday Discuss.* **2020**, *221*, 526–546.
- (38) Cheng, B.; Ceriotti, M. Computing the Absolute Gibbs Free Energy in Atomistic Simulations: Applications to Defects in Solids. *Phys. Rev. B* **2018**, *97*, No. 054102.
- (39) Artrith, N.; Urban, A. An Implementation of Artificial Neural-Network Potentials for Atomistic Materials Simulations: Performance for TiO₂. *Comput. Mater. Sci.* **2016**, *114*, 135–150.
- (40) Szlachta, W. J.; Bartók, A. P.; Csányi, G. Accuracy and Transferability of Gaussian Approximation Potential Models for Tungsten. *Phys. Rev. B* **2014**, *90*, No. 104108.
- (41) Bartók, A. P.; Kermode, J.; Bernstein, N.; Csányi, G. Machine Learning a General-Purpose Interatomic Potential for Silicon. *Phys. Rev. X* **2018**, *8*, No. 041048.
- (42) Shapeev, A. Moment Tensor Potentials: A Class of Systematically Improvable Interatomic Potentials. *Multiscale Model. Simul.* **2016**, *14*, 1153–1173.
- (43) Novikov, I. S.; Gubaev, K.; Podryabinkin, E.; Shapeev, A. V. The MLIP Package: Moment Tensor Potentials with MPI and Active Learning. *Mach. Learn.: Sci. Technol.* **2021**, *2*, No. 025002.
- (44) Nyshadham, C.; Rupp, M.; Bekker, B.; Shapeev, A. V.; Mueller, T.; Rosenbrock, C. W.; Csányi, G.; Wingate, D. W.; Hart, G. L. W. Machine-Learned Multi-System Surrogate Models for Materials Prediction. *npj Comput. Mater.* **2019**, *5*, No. 51.
- (45) Zuo, Y.; Chen, C.; Li, X.; Deng, Z.; Chen, Y.; Behler, J.; Csányi, G.; Shapeev, A. V.; Thompson, A. P.; Wood, M. A.; Ong, S. P. Performance and Cost Assessment of Machine Learning Interatomic Potentials. *J. Phys. Chem. A* **2020**, *124*, 731–745.
- (46) Podryabinkin, E. V.; Shapeev, A. V. Active Learning of Linearly Parametrized Interatomic Potentials. *Comput. Mater. Sci.* **2017**, *140*, 171–180.
- (47) Szlufarska, I. Atomistic Simulations of Nanoindentation. *Mater. Today* **2006**, *9*, 42–50.
- (48) Sushko, G. B.; Verkhovtsev, A. V.; Yakubovich, A. V.; Solovyov, A. V. Molecular Dynamics Simulation of Nanoindentation of Nickel-Titanium Crystal. *J. Phys.: Conf. Ser.* **2013**, *438*, No. 012021.
- (49) Plimpton, S. Fast Parallel Algorithms for Short-Range Molecular Dynamics. *J. Comput. Phys.* **1995**, *117*, 1–19.
- (50) Settles, B. *Active Learning Literature Survey*; Computer Sciences Technical Report 1648; University of Wisconsin—Madison, 2009.
- (51) Hodapp, M.; Shapeev, A. In Operando Active Learning of Interatomic Interaction during Large-Scale Simulations. *Mach. Learn.: Sci. Technol.* **2020**, *1*, No. 045005.
- (52) Bernstein, N.; Kermode, J. R.; Csányi, G. Hybrid Atomistic Simulation Methods for Materials Systems. *Rep. Prog. Phys.* **2009**, *72*, No. 026501.
- (53) Kresse, G.; Furthmüller, J. Efficiency of Ab-Initio Total Energy Calculations for Metals and Semiconductors Using a Plane-Wave Basis Set. *Comput. Mater. Sci.* **1996**, *6*, 15–50.
- (54) Blöchl, P. E. Projector Augmented-Wave Method. *Phys. Rev. B* **1994**, *50*, 17953–17979.
- (55) Kresse, G.; Joubert, D. From Ultrasoft Pseudopotentials to the Projector Augmented-Wave Method. *Phys. Rev. B* **1999**, *59*, 1758–1775.
- (56) Perdew, J. P.; Burke, K.; Ernzerhof, M. Generalized Gradient Approximation Made Simple. *Phys. Rev. Lett.* **1996**, *77*, 3865–3868.
- (57) Goreinov, S.; Oseledets, I.; Savostyanov, D.; Tyrtyshnikov, E.; Zamarashkin, N. How to Find a Good Submatrix. In *Matrix Methods: Theory, Algorithms, Applications*; World Scientific, 2010; pp 247–256.
- (58) Larsson, K. Simulation of Diamond Surface Chemistry: Reactivity and Properties. In *Some Aspects of Diamonds in Scientific Research and High Technology*; Lipatov, E., Ed.; IntechOpen, 2020.
- (59) Ristein, J. Surface Science of Diamond: Familiar and Amazing. *Surf. Sci.* **2006**, *600*, 3677–3689.
- (60) Denning, R. M. The Grinding Hardness of Diamond in a Principal Cutting Direction. *Am. Mineral.* **1957**, *42*, 362–366.
- (61) Dub, S.; Lytvyn, P.; Strelchuk, V.; Nikolenko, A.; Stubrov, Y.; Petrusha, I.; Taniguchi, T.; Ivakhnenko, S. Vickers Hardness of Diamond and CBN Single Crystals: AFM Approach. *Crystals* **2017**, *7*, No. 369.
- (62) Blank, V.; Popov, M.; Pivovarov, G.; Lvova, N.; Gogolinsky, K.; Reshetov, V. Ultrahard and Superhard Phases of Fullerite C₆₀: Comparison with Diamond on Hardness and Wear. *Diamond Relat. Mater.* **1998**, *7*, 427–431.
- (63) Eswar Prasad, K.; Ramesh, K. T. Hardness and Mechanical Anisotropy of Hexagonal SiC Single Crystal Polytypes. *J. Alloys Compd.* **2019**, *770*, 158–165.
- (64) Yonenaga, I.; Shima, T.; Sluiter, M. H. F. Nano-Indentation Hardness and Elastic Moduli of Bulk Single-Crystal AlN. *Jpn. J. Appl. Phys.* **2002**, *41*, 4620.
- (65) Jian, S.-R.; Chen, G.-J.; Lin, T.-C. Berkovich Nanoindentation on AlN Thin Films. *Nanoscale Res. Lett.* **2010**, *5*, No. 935.
- (66) Lech, A. T.; Turner, C. L.; Mohammadi, R.; Tolbert, S. H.; Kaner, R. B. Structure of Superhard Tungsten Tetraboride: A Missing Link between MB₂ and MB₁₂ Higher Borides. *Proc. Natl. Acad. Sci. U.S.A.* **2015**, *112*, 3223–3228.
- (67) Solozhenko, V. L.; Andrault, D.; Fiquet, G.; Mezouar, M.; Rubie, D. C. Synthesis of Superhard Cubic BC₂N. *Appl. Phys. Lett.* **2001**, *78*, 1385–1387.
- (68) Solozhenko, V. L.; Dub, S. N.; Novikov, N. V. Mechanical Properties of Cubic BC₂N, a New Superhard Phase. *Diamond Relat. Mater.* **2001**, *10*, 2228–2231.
- (69) Walls, M. G.; Chaudhri, M. M.; Tang, T. B. STM Profilometry of Low-Load Vickers Indentations in a Silicon Crystal. *J. Phys. D: Appl. Phys.* **1992**, *25*, 500–507.
- (70) Budnitzki, M.; Kuna, M. Experimental and Numerical Investigations on Stress Induced Phase Transitions in Silicon. *Int. J. Solids Struct.* **2017**, *106–107*, 294–304.
- (71) Domnich, V.; Aratyn, Y.; Kriven, W. M.; Gogotsi, Y. Temperature Dependence of Silicon Hardness: Experimental Evidence of Phase Transformation. *Rev. Adv. Mater. Sci.* **2008**, *17*, 33–41.